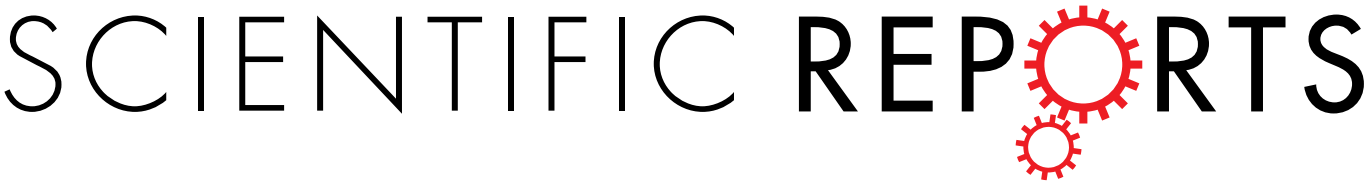

OPEN

A compact tunable polarized X-ray source based on laser-plasma helical undulators

Received: 31 March 2016
Accepted: 14 June 2016
Published: 05 July 2016

J. Luo[1,2], M. Chen[1,2], M. Zeng[1,2], J. Vieira[3], L. L. Yu[1,2], S. M. Weng[1,2], L. O. Silva[3], D. A. Jaroszynski[4], Z. M. Sheng[1,2,4] & J. Zhang[1,2]

Laser wakefield accelerators have great potential as the basis for next generation compact radiation sources because of their extremely high accelerating gradients. However, X-ray radiation from such devices still lacks tunability, especially of the intensity and polarization distributions. Here we propose a tunable polarized radiation source based on a helical plasma undulator in a plasma channel guided wakefield accelerator. When a laser pulse is initially incident with a skew angle relative to the channel axis, the laser and accelerated electrons experience collective spiral motions, which leads to elliptically polarized synchrotron-like radiation with flexible tunability on radiation intensity, spectra and polarization. We demonstrate that a radiation source with millimeter size and peak brilliance of 2×10^{19} photons/s/mm^2/mrad^2/0.1% bandwidth can be made with moderate laser and electron beam parameters. This brilliance is comparable with third generation synchrotron radiation facilities running at similar photon energies, suggesting that laser plasma based radiation sources are promising for advanced applications.

Tunable X-ray synchrotron radiation (SR) sources have wide applications in natural sciences, medicine and industry[1,2]. X-rays for such applications are mostly generated from SR facilities, which are usually bulky, costly and not able to satisfy the increasing demand for researches and applications[3]. Compact, tunable and flexible light sources are ideal for a broad range of applications and many schemes for such sources are under investigation[4,5]. Among these the laser wakefield accelerator (LWFA) scheme is highly promising due to its tremendous accelerating gradient[6–8]. Electrons can be longitudinally accelerated to GeV energies over centimeters[9]. Besides longitudinal acceleration, electrons also undergo transverse betatron oscillations in wakefields, which lead to the emission of electromagnetic radiation in the X-ray range[10–12]. Applications of these radiation sources such as object imaging with high resolution have already been tested[13–15]. Further applications may become possible if some key properties of these radiation sources, such as brightness, spectral features and polarization, can be controlled. Among these the polarization is relatively more difficult to control as it relies on the polarization of the electron betatron motion. However, it is usually transversely isotropic. Although the polarization can be controlled through electron injection selection or driver pulse tilting techniques[16,17], the polarization tunability is still not sufficient. Coupling the LWFA with external magnetic undulators would produce tunable radiation. However, both the operation difficulty and the device size increase. External undulators and beam transport systems would enlarge the size of the devices from centimetres to several meters[18].

Making a more compact radiation source with both small acceleration and radiation lengths is challenging. In order to reach this goal, many kinds of plasma based undulators with small period length have been suggested as possible candidates to replace conventional magnetic undulators[19–25]. Among them Rykovanov *et al.* have studied the properties of a laser plasma based undulator and the radiation of an external injected electron beam in detail, which shows the potential for future extremely compact free-electron laser (FEL) applications[23]. Besides the compactness, such a laser-plasma-based undulator may offer great flexibility and tunability. For example, polarization control of the plasma undulator may be achieved by the direction of the initial laser pulse centroid displacement,

[1]Key Laboratory for Laser Plasmas (Ministry of Education) and Department of Physics and Astronomy, Shanghai Jiao Tong University, Shanghai, 200240, China. [2]Collaborative Innovation Center of IFSA (CICIFSA), Shanghai Jiao Tong University, Shanghai, 200240, China. [3]GoLP/Instituto de Plasmas e Fusao Nuclear, Instituto Superior Tecnico, Universidade de Lisboa, Lisbon, 1049-001, Portugal. [4]SUPA, Department of Physics, University of Strathclyde, Glasgow, G4 0NG, UK. Correspondence and requests for materials should be addressed to M.C. (email: minchen@sjtu.edu.cn) or Z.M.S. (email: z.sheng@strath.ac.uk)

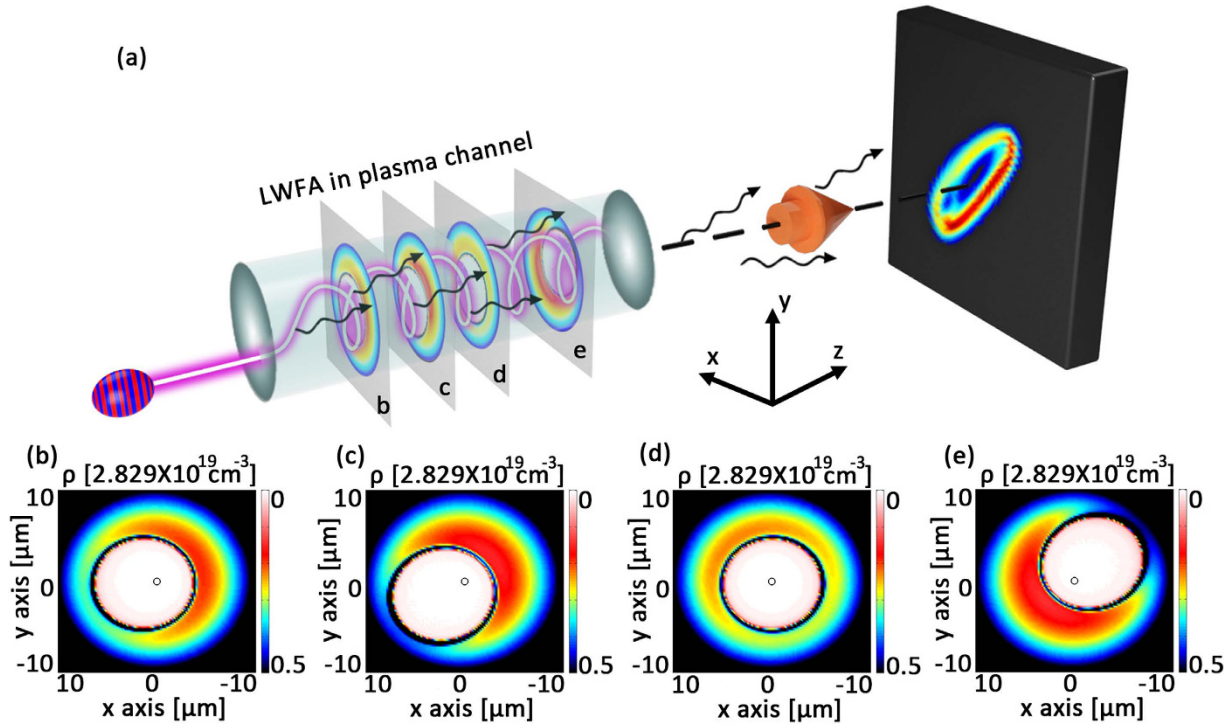

Figure 1. Sketch of the radiation source from a helical plasma undulator based on LWFA. (**a**) Spiral motion of laser pulse, wakefield in the plasma channel and the far field X-ray radiation distribution. (**b**–**e**) are the electron density distributions of the transverse slices of the accelerating bubble structure with largest radius at t = 133 fs (**b**), t = 600 fs (**c**), t = 1200 fs (**d**), t = 1800 fs (**e**).

and elliptical polarization with arbitrary ellipticity can be produced by injecting the laser pulse into the channel off axis and at an angle. Here, we extend these studies by including the electron beams acceleration process and using three dimensional Particle-in-Cell (3D-PIC) simulations to include the laser propagation, wake acceleration processes and show the tunability of radiation from such a laser plasma based helical plasma undulator for the first time, thus paving the way to more flexible and controllable X-ray generation. Through the simulations we show clearly that the motion of the laser inside the plasma channel depends on the initial incidence offset position and angle between the laser and channel axis. We find conditions when the laser spirals about the channel axis, thereby leading to helical betatron trajectories of accelerated electrons. A post radiation calculation code was used to study the X-ray emission in the far field. Besides the intensity distribution, we find that the polarization and spectra of the radiation are easily controllable by changing the incidence of the driver pulse and channel profiles. Considering typical laser plasma parameters, currently available in many laboratories, we find that our centimeter scale, plasma-based radiation source is expected to deliver ultra-intense X-rays, with peak brilliance as large as 2×10^{19} photons/s/mm^2/mrad^2/0.1% bandwidth. Such high quality flexible and compact radiation sources have the potential to benefit a wide variety of applications.

Results and Discussions

Laser and electron beam spiral motions inside the plasma channel. We first study the electron motion inside the plasma channel which resembles that in a helical undulator. Stable LWFA usually use plasma channels to guide the laser pulse over many Rayleigh lengths (i.e. $Z_R = k_0 w_0^2/2$, where $k_0 = 2\pi/\lambda_0$ is the laser wave number, w_0 is the focal spot size and λ_0 is the laser wavelength). A plasma channel with a transverse density profile of $n(r) = n_0 + \Delta n r^2/r_0^2$ can guide the laser for long distances, where r represents the transverse coordinate, n_0 is the on-axis electron density, Δn is the channel depth and r_0 is the channel width[7,22,23]. For a matched channel (i.e., $\Delta n = \Delta n_c = (\pi r_e r_0^2)^{-1}$ and $r_0 = w_0$, where $r_e = e^2/m_e c^2$ is the classical electron radius with e and m_e the electron charge and mass at rest, respectively, and c the light speed in vacuum), the laser spot size remains approximately constant during all propagation. If a laser pulse is off-axially injected into the plasma channel or at some injection angle, the laser centroid will oscillate transversely in a single plane as it propagates forward[22]. The oscillation period length, given by $\Lambda_{os} = 2\pi Z_M (\Delta n_c/\Delta n)^{1/2}$, where $Z_M = \pi r_0^2/\lambda_0$, can be controlled by tuning the channel depth[22]. In addition, when the laser propagation direction is non-collinear with the channel axis, the laser centroid will perform a spiral trajectory around the channel axis as shown in Fig. 1(a). The centroid trajectory can be approximated from the eikonal equations[26] (refer to Supplementary Material). In cylindrical coordinates (r, ϕ, z), the laser centroid trajectory is given by

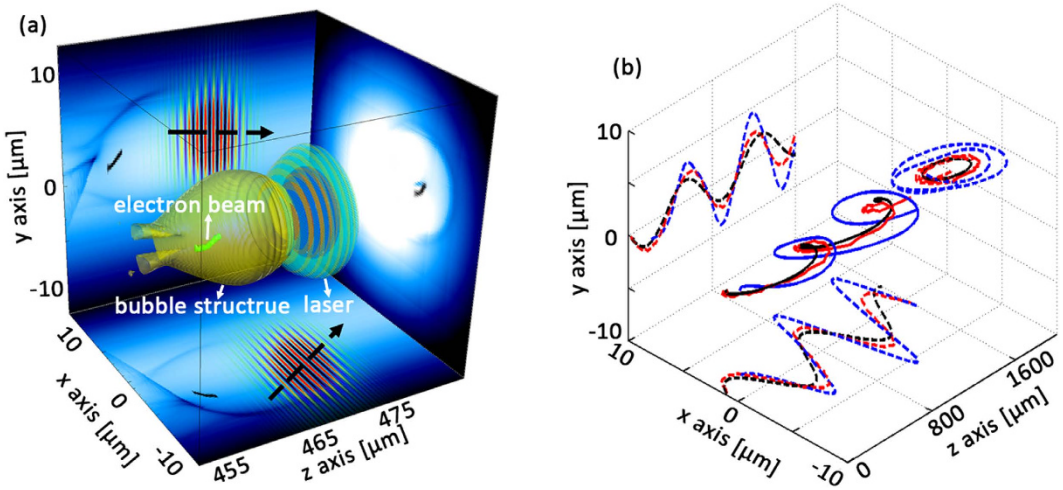

Figure 2. Spiral motions of the laser pulse and electron beam in the plasma channel. (**a**) A snapshot of plasma density (blue background), bubble structure (yellow surface), injected electron beam (light green points), and laser electric fields (blue-red-orange-green iso-surfaces and the projections). The black dashed arrows show the laser propagation direction in projection planes. (**b**) Theoretical (black solid line) and simulation (red solid line) results of the laser pulse centroid trajectory. The blue solid line shows the centroid trajectory of the traced particles. Dashed lines are the projections of the trajectories.

$$\frac{dr}{dz} = \pm \frac{1}{\cos\theta_z}\left[1 - \frac{n(r)}{n_c} - \left(1 - \frac{n_{e0}}{n_c}\right)\cdot\left(\sin^2\theta_z \frac{b^2}{r^2} + \cos^2\theta_z\right)\right]^{1/2} \quad (1)$$

$$\frac{d\phi}{dz} = \frac{b\ \sin\theta_z}{r^2\ \cos\theta_z} \quad (2)$$

with $\theta_z = \arccos\left(\sqrt{1 - \cos^2\theta_x - \cos^2\theta_y}\right)$, and where $\theta_{x,y,z}$ are the angles between the laser propagation direction and the space coordinate axes x, y, and z. Moreover, n_c is the critical density of plasma, $n_{e0} = n_e\left(r = \sqrt{x_0^2 + y_0^2}\right)$ is the plasma density at the laser incidence point (x_0, y_0). The parameter $b = \left(y_0 - x_0\ \cos\theta_y/\cos\theta_x\right)/\left(\sqrt{\left(\cos\theta_y/\cos\theta_x\right)^2 + 1}\right)$ is the distance between the projection of the incident laser pulse and the plasma channel centre.

When an ultrashort, ultraintense laser pulse propagates in such a plasma channel, the background electrons are expelled outward due to the pondermotive force of the driver, generating bubble like wakefields[27,28]. If the laser pulse oscillates transversely, the bubble will follow the laser, forcing electrons inside the bubble to follow the motion of the laser centroid[20]. The oscillation period and amplitude can be kept constant until near the laser pump depletion[22]. Thus the plasma acts as a helical undulator and the radiation of the electrons shows typical helical undulator radiation properties, which are dramatically different from those of normal betatron radiation.

We used the fully-relativistic PIC code OSIRIS[29] to investigate the self-consistent 3D dynamics of the laser centroid motion and electron acceleration inside the plasma channel when the laser wave vector is not aligned with the channel axis. Detailed simulation parameters can be found in the Methods. The channel axis is set along the z axis. In a typical simulation shown in Fig. 1, the initial parameters of laser incidence are $x_0 = 1\ \mu m$, $y_0 = 0$, $\theta_x = 89°$ and $\theta_y = 91°$. Typical bubble cross sections at different laser propagation distances are plotted in Fig. 1(b–e). Figure 2(a) shows a typical snapshot of the 3D structure of the laser driven blowout region (yellow), with the externally injected electrons at the back of the bubble (light green), and the laser electric fields (blue-red-orange-dark green). Projections of the laser propagation direction on x-y and x-z planes (black dashed arrows) in Fig. 2(a) and a movie of the laser and wake evolution (refer to the Supplementary Material) indicate the spiral motion. The black solid lines in Fig. 2(b) shows typical trajectory of the laser centroid obtained from theoretical approximations by solving Eqs (1) and (2). The red solid line represents the trajectory from 3D-PIC simulations. The dashed lines on the side planes are the corresponding trajectory projections. The analytical model correctly predicts the wavelength and amplitude of the laser centroid oscillations, both in good agreement with PIC simulations. These results show that the eikonal equations can be used to describe the laser propagation for the typical propagation distances in our investigation. The oscillation wavelength from the PIC simulation is about 700 μm closed to the theoretical approximation $\Lambda_{os} = 719.5\ \mu m$. In the simulations, because of the laser energy depletion and frequency red shifting as the pulse propagates further, the oscillation wavelength and amplitude become smaller than theoretical predictions. Besides, by comparing laser centroid trajectories and electron beam centroid trajectories with $a_0 = 2$ and $a_0 = 0.5$ (see Supplementary Material), we found relativistic non-linear

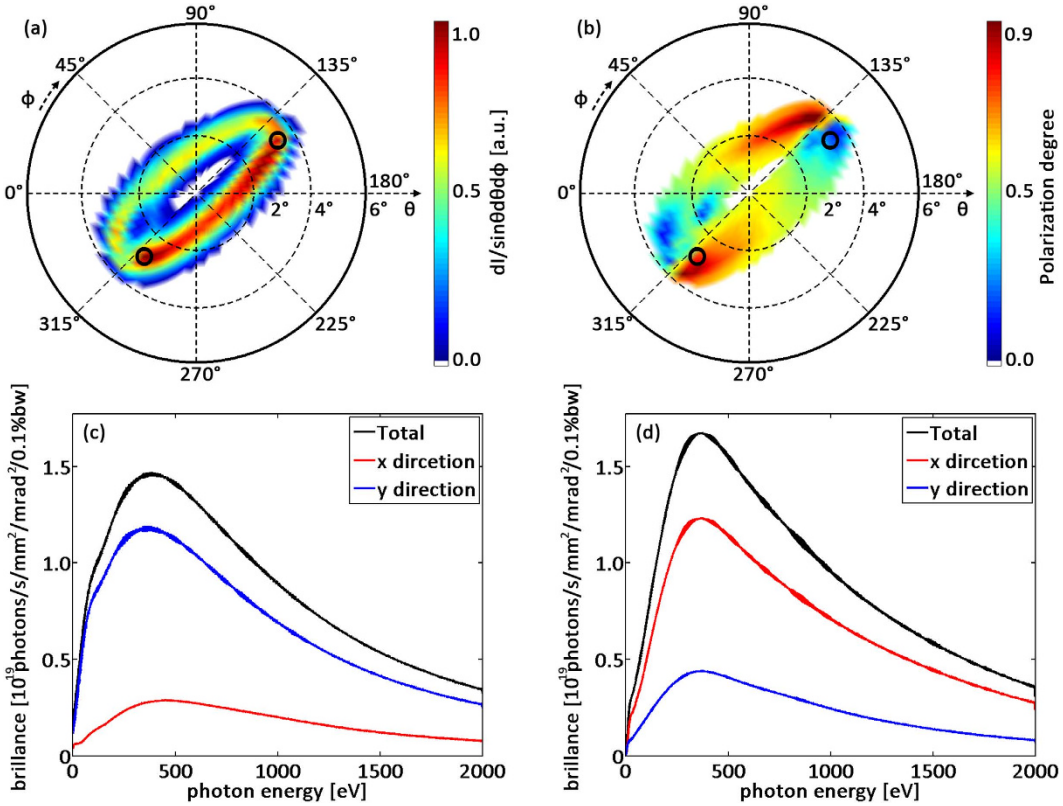

Figure 3. Intensity and polarization distributions of X-ray radiation. (**a**) Far field radiation intensity distribution, (**b**) polarization distribution, (**c**) radiation spectrum of the marked upper right point and lower left point (**d**).

effects appears when $a_0 = 2$ where trajectories deviate from theoretical evaluations. However, the general trend remains similar and the helical motion of such trajectories is still predicable.

To reduce simulation time and concentrate on the study of the properties of the radiation emitted by the trapped electrons, we consider an external injected scenario, employing a cylindrical electron beam to study the radiation dependance on the intial laser incidence. An illustration of a simulation including ionization injection is given in the Supplementary Material, in order to illustrate the feasibility of our scheme in an all optical setup by only using LWFA. As mentioned before, the trapped and accelerated electron beam experiences spiral motion simutaneously with the acceleration structure following the laser pulse inside the plasma channel. We randomly traced 200 particles from the accelerated electron beam. The centroid position of these electrons (x_c, y_c, z_c) are shown in Fig. 2(b) by the blue solid line. As one can see, the period of the spiral motion of the electrons closely follows the period of the laser centroid oscillations. In addition, the amplitude of the oscillations is slightly higher than the laser centroid oscillations, due to its inertia. Electrons are accelerated to nearly 140 MeV in only 1600 μm. The rms deviation of the average energy increases to about 8 MeV, which results from the nonumiformity of the longitudinal acceleration fields in the helically moving bubble. The continuous acceleration of electrons with a stable accelerating gradient about 80 GeV/m before $x = 1600\ \mu m$ illustrates that electrons propagate near the back of the bubble. After $x > 1600\ \mu m$, the accelerating gradient reduces rapidly as electrons enter the dephasing region. So the following calculation of electrons trajectories and radiation stops at $x = 1600\ \mu m$, which corresponds to using a short capillary in practice.

X-ray radiation from the helical plasma undulator. The spiral motion of the trapped electrons inside the wakefield resembles the electron motion in a traditional helical undulator, which is common in a storage ring of a synchrotron facility for polarized X-ray emission[30]. We studied the radiation properties of these electrons with the numerical radiation post-processing code VDSR[31] (see Methods). This code calculates the radiation distribution according to electrons trajectories obtained from the 3D-PIC OSIRIS simulations. At the beginning of the electron acceleration the normal beam betatron period inside the accelerating bubble ($\lambda_\beta \approx \sqrt{2\gamma}\,\lambda_p$) is far smaller than the laser oscillation period (Λ_{os}), the radiation properties are more relied on the betatron motion and the emitted photons are low energies which are not the ones we are interested in. In the radiation calculations we cut out these low energy radiation part. Figure 3(a) shows the radiation intensity distribution captured by a virtual radiation detector located in the far-field and centred along the plasma channel axis (see schematic view in Fig. 1(a)). The initial injection parameters of the laser are the same as those in Fig. 1. The far field radiation pattern illustrated in Fig. 3(a) shows a hollow elliptical shape, which is consistent with the electron trajectories whose projection on x-y plane is shown in Fig. 2(b). Key properties of the radiation intensity distribution are described

by a fundamental dimensionless radiation parameter, called the strength parameter, given by $K = 2\pi\gamma r_{os}/\Lambda_{os}$, where γ is the Lorentz factor of the electrons, r_{os} is their transverse oscillation amplitude and Λ_{os} is the spiral motion period. In this case the electrons are rapidly accelerated to high energies ($\gamma \approx 274$). Moreover, the minimum oscillation amplitude is $(r_{os})_{min} \approx 1.41\ \mu m$, the maximum oscillation is $(r_{os})_{max} \approx 6.84\ \mu m$, and $\Lambda_{os} \approx 700\ \mu m$. These parameters leads to a minimum strength parameter $K_{min} \approx 3.5$ and a maximum $K_{max} \approx 16.8$. Both K_{min} and K_{max} are larger than unity, which means the radiation is in the wiggler regime. As a result, the radiation spectrum is broadband. The X-rays propagate along the emission angles $\theta \sim K/\gamma \approx 0.73°$ and 3.51°. These angles are larger than the angular width around the emission angle $\Delta \sim 1/\gamma \approx 0.21°$, therefore leading to the hollow intensity pattern shown in Fig. 3(a). Besides, more photons are emitted in Fig. 3(a) with azimuth angle ϕ between 135° and 315°. This is because the centroid trajectory of the electron beam ends in such azimuth angle range as well (see Fig. 2(b)). In our scheme, electrons are accelerated and radiate simultaneously. Thus, more intense high frequency radiation is produced when electrons have higher energy. A longer dephasing distance can lead more oscillation times of the electron beam and the impact of electron energy growth on the nonuniformity of the azimuthal angular distribution of the radiation would decrease.

To investigate the spectral properties, we have selected two points with the highest radiation intensities and marked them with black circles. As one can see, the maximum radiation intensity comes from the major axis vertices of the radiation ellipse with emission angle about $\theta \approx 3.5°$, which corresponds to the positions in the electron trajectory projection plane where the electrons have maximum deviation ($r_{os} \approx (r_{os})_{max}$) and experience maximum transverse acceleration. The photon energy spectra of the marked points are shown in Fig. 3(c,d). The peak position of the spectrum radiated along this direction is about 400 eV, which is about the average value of the on-axis radiation where the peak radiation energy is $E_p = \frac{3}{2}K\gamma^2 hc/\Lambda_{os} = 3\pi\gamma^3 r_{os} hc/\Lambda_{os}^2$ with h representing the Plancks constant[10]. For average electron energy ($\overline{\gamma} = 137$) it is $E_p = 418.9\ eV$. In addition, the energy spectra for the point with lowest radiation intensity and integrated over the entire observe region are given in the Supplementary Material.

In order to discuss the polarization properties of the radiated photons, we define the polarization direction degree of a point as $P = I_x/I_t$, where I_x is the radiation intensity with photon polarization in the x direction and I_t is the total radiation intensity. When $P = 1$ the radiation is linearly polarized in the x direction, while when $P = 0$ the radiation is linearly polarized in the y direction. The polarization direction degree distribution is shown in Fig. 3(b). The two points marked in Fig. 3(a) were also lined out. During the spiral motion, the directions of the electrons' transverse velocities keep changing, and so does the radiation polarization direction. The polarization direction degree appears to change periodically along the elliptical orbit. When electrons move to the upper right marked position, its velocity gradient component in the x direction is lower than that in the y direction, so $P < 0.5$ and the radiation intensity in the x direction (corresponding to red line in Fig. 3(c)) is weaker than that in the y direction (blue line in Fig. 3(c)). The opposite situation at the lower left marked position is shown in Fig. 3(d).

In addition to the polarization, the radiation intensity is also another important parameter for useful photon sources. The radiation intensity is proportional to the total number of electrons in the beam for incoherent emission. In our typical 3D-PIC simulations, due to the limitation of computational resources, small laser focal spot sizes and injected electron beam radii have been used. The externally injected beam charge used in the simulation is thus 4.5 pC, which is close to the ionization induced injection charge measured in the simulation reported in the Supplementary Material. With this charge, the totally number of radiated photons is about 2×10^7. A much larger photon number would be radiated if the total number of trapped electrons could be higher. In general, higher charges can be accelerated when using higher energy drivers propagating in lower density plasma in comparison to those considered in our work. Higher accelerated beam charge could also be obtained in ionization injection scenarios by increasing the concentration of the injection gas component. Considering the electron rotation transverse area 15.1 μm^2 and the bunch duration 6.67 fs, in our case the final peak radiation brightness is about 2×10^{19} photons/s/mm^2/mrad^2/0.1% bandwidth, which is comparable with the highest levels of current third generation of SR facilities at similar X-ray energies. However, compared to some newest studies on plasma based radiation sources, such as betatron radiation[32] and Thomson scattering radiation[33], the total photon number and the maximum radiation brightness in our present simulations are relatively small. In our scheme, the radiation region (several rad^2) is much larger than those found in other mechanisms (hundreds of $mrad^2$). Although this feature significantly lowers the maximum radiation brightness, the tunable radiation pattern in far field found here is unique and may find some special applications in addition to normal imaging. Moreover, the radiated photon number can be enhanced by using a larger laser spot size, increasing the oscillation number, or increasing the injected electron beam charge.

In our scheme the intensity and polarization distributions of the radiation can be easily controlled by varying the initial laser incidence parameters, i.e. the initial off-axis position (x_0, y_0) and the tilted injection angles (θ_x, θ_y). In Fig. 4(a) the laser centroid trajectories with different initial parameters are shown. The black line corresponds to the one shown in Fig. 2. The radiation shows hollow elliptical shape. An additional simulation was also performed in order to obtain a hollow and circular intensity profile by using laser injection parameters of $x_0 = 2.92\ \mu m$, $y_0 = 0$, and $\theta_x = 90°$, $\theta_y = 91.5°$. The laser performs circular rotation around the channel axis initially. Near laser pump depletion, however, radius of rotation decreases as shown by the red line in Fig. 4(a). Because the emission angle is larger than the angular width of the radiation, the radiation intensity distribution also exhibits a hollow circle pattern, illustrated in Fig. 4(b). The corresponding radiation polarization distribution is shown in Fig. 4(c). As one can see the polarization changes along the azimuthal direction. This kind of distribution is very convenient for many light-polarization-dependent applications.

Quasi linearly polarized X-rays can also be generated by selecting appropriate initial laser incidence. If one fixes the initial incidence position ($x_0 = 1\ \mu m$, $y_0 = 0$), and incidence angle $\theta_y = 91°$, but only decreases θ_x from 89° to 88°, the ellipticity decrease of the laser centroid trajectory is evident from the blue line in Fig. 4(a).

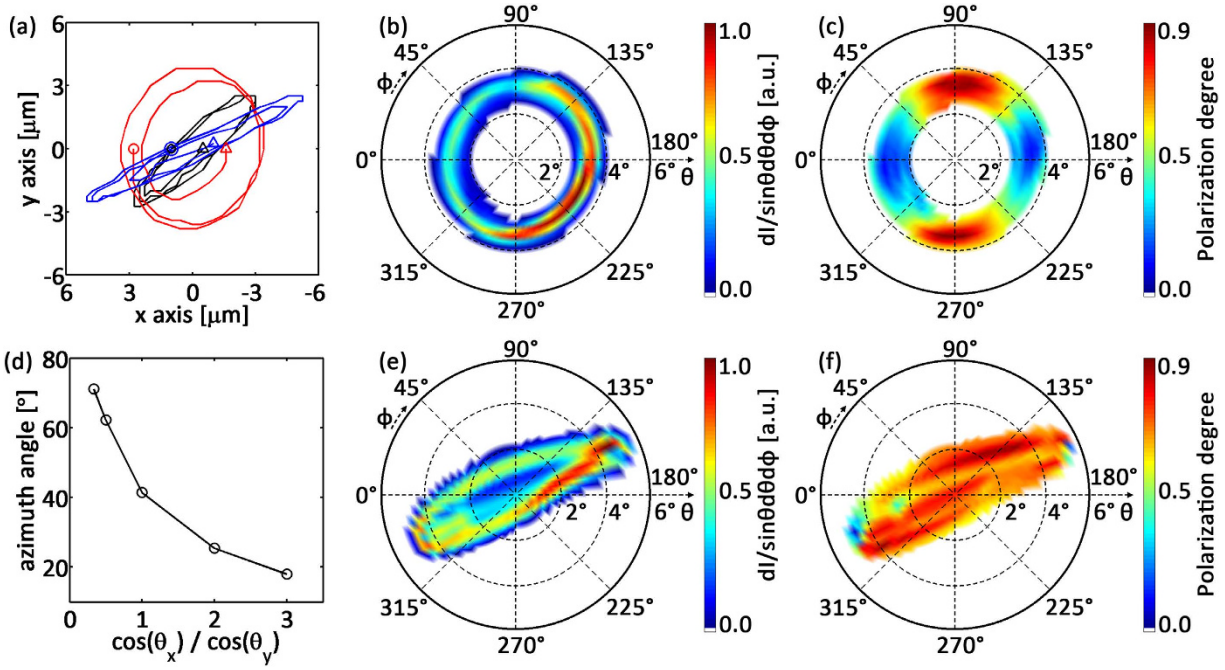

Figure 4. Radiation distributions of intensity and polarization for different laser incidence parameters. (**a**) Laser centroid trajectories on x-y plane with initial laser incidence parameters of $x_0 = 1\ \mu m$, $\theta_x = 89°$, $\theta_y = 91°$ (black), $x_0 = 2.92\ \mu m$, $\theta_x = 90°$, $\theta_y = 91.5°$ (red), and $x_0 = 1\ \mu m$, $\theta_x = 88°$, $\theta_y = 91°$. Input parameter y_0 is fixed to be $0\ \mu m$. The circles and triangles mark the start and end positions of these trajectories, respectively. (**b**,**e**) are radiation intensity distributions and (**c**,**f**) are radiation polarization distributions. (**b**,**c**) correspond to the red line in (**a**), (**e**,**f**) correspond to blue line in (**a**). (**d**) The correlation between the azimuth angle of the elliptical radiation region and the ratio of the cosine function of incidence parameters θ_x and θ_y.

Correspondingly the electron radiation intensity distribution shows a linear structure (shown in Fig. 4(e)) and a bigger radiation polarization degree P is obtained (see Fig. 4(f)), which means that most of the radiated photons are linearly polarized. Furthermore, in this simulation the oscillation amplitude of the electrons has been increased as one can see in Fig. 4(a). The strength parameter (K) is then increased as well. We find that with these parameters the final peak photon energy moves to 1.5 keV, which shows the tunability of radiation energy. Another way to tune the radiation energy is by varying the channel depth since the strength parameter depends on the laser oscillation period in the parabolic plasma channel. The effects of the channel depth on the radiation parameters has already been studied in detail in refs 22 and 23.

In general, fine tunability of the distribution of the radiation intensity and polarization can be obtained by controlling the combinations of the initial laser incidence parameters. Here we only show the tunability of the elliptical azimuth angle of the radiation pattern by controlling the combined parameter of $\cos(\theta_x)/\cos(\theta_y)$ with fixed incidence position (x_0, y_0). The results are shown in Fig. 4(d). The radiation tilt angle can be tuned from 20 to 70 degrees freely. Because of the coincidence of the electron motion and the laser centroid motion, in practice, one can design the radiation properties by solving the eikonal equations of the laser motion first.

Conclusion

In conclusion, we have studied highly tunable soft X-ray radiation from a helical plasma undulator based on LWFA in a plasma channel. The plasma can act as a helical undulator modulating electron motion, such that elliptically polarized synchrotron radiation can be produced. By controlling the laser incidence parameters and the profile of the plasma channel, the oscillation amplitude of the accelerated electrons, the shape and the azimuth angle of the elliptical radiation region, and the radiation polarization can all be adjusted. This would give a more flexible tunability of the distribution of the final radiation intensity, spectrum and the polarization. To our knowledge, such high controllability and tunability of the produced radiation has not been realized in usual LWFA based betatron radiation scheme[34,35]. In general X-ray radiations with hollow elliptical shape and elliptical polarization with brightness comparable to or even higher than the third generation of synchrotron radiation sources can be obtained from these plasma based helical undulators. Our studies reveal that such all optical-plasma compact radiation sources can be made highly flexible and are therefore suitable for advanced applications, such as soft X-ray spectromicroscopy[36] or atomic and molecular physics[37]. Although currently there are still many issues such as average photon flux, spectrum width, and stability to be improved, the recent progresses on wakefield acceleration (i.e. ionization injection[38,39], cold optical injection[40], transverse optical injection[41], wake diagnosis[42] and high repetition lasers[43,44]) have shown their great potential to make more stable, high quality and high flux radiation sources.

Methods

Particle-in-Cell simulations. 3D-PIC simulations were performed with OSIRIS code. In the simulations, the profile of the normalized laser vector potential is given by $a = eA/m_e c^2 = a_0 \times \exp(-t^2/L_0^2 - r^2/w_0^2)$ with $a_0 = 2.0$ (corresponding to the peak intensity of the polarized laser pulse of $I = 8.6 \times 10^{18}\, W/cm^2$), $L_0 = 4.0\ T_0$, $w_0 = 6.75\ \lambda_0$ and the laser wavelength $\lambda_0 = 0.8\,\mu m$, the laser period $T_0 = 2\pi/\omega_0 \approx 2.67$ fs. The plasma density has a parabolic profile with $n_0 = 0.001\ n_c$, $\Delta n = \Delta n_c$, $r_0 = w_0$, where $n_c \approx 1.7 \times 10^{21}\, cm^{-3}$ is the critical plasma density for the driver pulse. The injected external electron beam has transverse and longitudinal dimensions with size of $L_r = 0.5\,\mu m$, $L_z = 2.0\,\mu m$, and a charge of $Q \approx 4.5$ pC. The energy of the beam is $E_e = 7.7$ MeV or 5.1 MeV in different simulation cases. The size of the simulation box is $40 \times 40 \times 45\ \mu m^3$ corresponding to cell size of $200 \times 200 \times 1035$. We use 4 super-particles per cell and 8 super-particles per cell for the background electrons and external injected electrons, respectively.

Radiation calculations. Post process code VDSR was used to perform the radiation calculation. The spatial and velocity vectors of 200 super-particles randomly selected from the accelerated electron beam in 3D-PIC simulations were input into the VDSR code. The time internal of trajectory recording is $dt = 0.04\ T_0$. The code integrates each particle's radiation along its trajectory. Since the electron beam size is much longer compared with the radiation wavelength interested here, the radiation is essentially incoherent. Because of the computational source limitation, the number of the traced particle is too small for a coherent addition of the electron radiation, we then sum them incoherently to get the final far field spectra on a virtual screen with spatial resolutions. The detected circular region covers a maximum polar angle of 6°, which is divided into 24 parts in the radial direction and 72 parts in the azimuthal direction.

References

1. Huxley, H. E. *et al.* The use of synchrotron radiation in time-resolved X-ray diffraction studies of myosin layer-line reflections during muscle contraction. *Nature* **284,** 140–143 (1980).
2. Chen, L., Dürr, K. L. & Gouaux, E. X-ray structures of AMPA receptor-cone snail toxin complexes illuminate activation mechanism. *Science* **345,** 1021–1026 (2014).
3. Bilderback, D. H., Elleaume, P. & Weckert, E. Review of third and next generation synchrotron light sources. *J. Phys. B At. Mol. Opt. Phys.* **38,** S773–S797 (2005).
4. Wong, L. J. *et al.* Towards grapheme plasmon-based free-electron infrared to X-ray sources. *Nature Photon.* **10,** 46–52 (2016).
5. Phuoc, K. T. *et al.* Laser based synchrotron radiation. *Phys. Plasmas* **12,** 023101 (2005).
6. Tajima, T. & Dawson, J. M. Laser Electron Accelerator. *Phys. Rev. Lett.* **43,** 267–270 (1979).
7. Esarey, E., Schroeder, C. B. & Leemans, W. P. Physics of laser-driven plasma-based electron accelerators. *Rev. Mod. Phys.* **81,** 1229–1285 (2009).
8. Hooker, S. M. Developments in laser-driven plasma accelerators. *Nature Photon.* **7,** 775–782 (2013).
9. Leemans, W. P. *et al.* Multi-GeV electron beams from capillary-discharge-guided subpetawatt laser pulses in the self-trapping regime. *Phys. Rev. Lett.* **113,** 245002 (2014).
10. Corde, S. *et al.* Femtosecond x rays from laser-plasma accelerators. *Rev. Mod. Phys.* **85,** 1–48 (2013).
11. Rousse, A. *et al.* Production of a keV X-ray beam from synchrotron radiation in relativistic laser-plasma interaction. *Phys. Rev. Lett.* **93,** 135005 (2004).
12. Cipiccia, S. *et al.* Gamma-rays from harmonically resonant betatron oscillations in a plasma wake. *Nature Phys.* **7,** 867–871 (2011).
13. Fourmaux, S. *et al.* Single shot phase contrast imaging using laser-produced Betatron X-ray beams. *Opt. Lett.* **36,** 2426–2428 (2011).
14. Kneip, S. *et al.* X-ray phase contrast imaging of biological specimens with femtosecond pulses of betatron radiation from a compact laser plasma wakefield accelerator. *Appl. Phys. Lett.* **99,** 093701 (2011).
15. Wenz, J. *et al.* Quantitative X-ray phase-contrast microtomography from a compact laser-driven betatron source. *Nature Commun.* **6,** 7568 (2015).
16. Schnell, M. *et al.* Optical control of hard X-ray polarization by electron injection in a laser wakefield accelerator. *Nature Commun.* **4,** 2421 (2013).
17. Popp, A. *et al.* All-optical steering of laser-wakefield-accelerated electron beams. *Phys. Rev. Lett.* **105,** 215001 (2010).
18. Schlenvoigt, H.-P. *et al.* A compact synchrotron radiation source driven by a laser-plasma wakefield accelerator. *Nature Phys.* **4,** 130 (2008).
19. Joshi, C. *et al.* Plasma wave wigglers for free-electron lasers. *IEEE J. Quantum Electron.* **23,** 1571–1577 (1987).
20. Reitsma, A. & Jaroszynski, D. Propagation of a short intense laser pulse in a curve plasma channel. *IEEE Trans. Plasma Sci.* **36,** 1738–1745 (2008).
21. Andriyash, I. A. *et al.* An ultracompact X-ray source based on a laser-plasma undulator. *Nature. Commun.* **5,** 4736 (2014).
22. Chen, M. *et al.* Tunable synchrotron-like radiation from centimetre scale plasma channels. *Light Sci. Appl.* **5,** e16015 (2016).
23. Rykovanov, S. G. *et al.* Plasma undulator based on laser excitation of wakefields in a plasma channel. *Phys. Rev. Lett.* **114,** 145003 (2015).
24. Vieira, J. *et al.* Plasma based helical undulator for controlled emission of circularly and elliptically polarised betatron radiation. arXiv:1601.04422v1 (2016).
25. Hooker, S. M., Gonsalves, A. J., Jaroszynski, D. A. & Leemans, W. P. Charged particle accelerator and radiation source. U.S. Patent No. 8299713, Oct. 30, 2012.
26. Born, M. & Wolf, E. *Principles of Optics* (Oxford Dergamon Press, 1975).
27. Pukhov, A. & Meyer-ter-Vehn, J. Laser wake field acceleration: the highly non-linear broken-wave regime. *Appl. Phys. B* **74,** 355–361 (2002).
28. Lu, W. *et al.* Generating multi-GeV electron bunches using single stage laser wakefield acceleration in a 3D nonlinear regime. *Phys. Rev. ST Accel. Beams* **10,** 061301 (2007).
29. Fonseca, R. A. *et al.* OSIRIS: A three-dimensional fully relativistic particle in cell code for modeling plasma based accelerators. *Lect. Notes Comp. Sci.* **2331,** 342–351 (2002).
30. Wang, C.-X. & Schlueter, R. Optimization of circularly-polarized radiation from an elliptical wiggler, asymmetric wiggler, or bending magnet. *Nucl. Instr. Meth. In Phys. Rev. A* **347,** 92–97 (1994).
31. Chen, M. *et al.* Modeling classical and quantum radiation from laser-plasma accelerators. *Phys. Rev. ST Accel. Beams* **16,** 030701 (2013).
32. Kneip, S. *et al.* Bright spatially coherent synchrotron X-rays from a table-top source. *Nature Phys.* **6,** 980–983 (2010).
33. Khrennikov, K. *et al.* Tunable all-optical quasimonochromatic Thomson X-ray source in the nonlinear regime. *Phys. Rev. Lett.* **114,** 195003 (2015).

34. Phuoc, K. T. *et al.* Imaging electron trajectories in a laser-wakefield cavity using betatron X-ray radiation. *Phys. Rev. Lett.* **97,** 225002 (2006).
35. Albert, F. *et al.* Angular dependence of betatron X-ray spectra from a laser-wakefield accelerator. *Phys. Rev. Lett.* **111,** 235004 (2013).
36. Xue, C. *et al.* High-performance soft X-ray spectromicroscopy beamline at SSRF. *Rev. Sci. Instrum.* **81,** 103502 (2010).
37. Lebech, M. *et al.* Complete description of linear molecule photoionization achieved by vector correlations using the light of a single circular polarization. *J. Chem. Phys.* **118,** 9653–9663 (2003).
38. Pak, A. *et al.* Injection and trapping of tunnel-ionized electrons into laser-produced wakes. *Phys. Rev. Lett.* **104,** 025003 (2010).
39. Zeng, M. *et al.* Multichromatic Narrow-Energy-Spread Electron Bunches from Laser-Wakefield Acceleration with Dual-Color Lasers. *Phys. Rev. Lett.* **114,** 084801 (2015).
40. Davoine, X. *et al.* Cold optical injection producing monoenergetic, multi-GeV electron bunches. *Phys. Rev. Lett.* **102,** 065001 (2009).
41. Lehe, R. *et al.* Optical transverse injection in laser-plasma acceleration. *Phys. Rev. Lett.* **111,** 085005 (2013).
42. Matlis, N. H. *et al.* Snapshots of laser wakefields. *Nature Phys.* **2,** 749–753 (2006).
43. Schmid, K. *et al.* Few-cycle laser-driven electron acceleration. *Phys. Rev. Lett.* **102,** 124801 (2009).
44. Mourou, G. *et al.* The future is fibre accelerators. *Nature Photon.* **4,** 258–261 (2013).

Acknowledgements

This work is supported in part by the National Basic Research Program of China (2013CBA01504), the National Science Foundation of China (11421064, 11374209, 11374210), a MOST international collaboration project (2014DFG02330), and an EU Horizon 2020 Programme project EuPRAXIA (Grant No. 653782). M.C. appreciates supports from National 1000 Young Talent Program. J.V. and L.O.S. acknowledge Laserlab 3 (Contract No. 284464) and Laserlab 4 (Contract No. 654148). D.A.J. and Z.M.S. acknowledge support of the U.K. EPSRC (Grant No. EP/J018171/1 and EP/N028694/1), Laserlab (Grant No. 654148), EuCARD-2 (Grant No. 312453), and a Leverhulme Trust Research Grant. The authors would like to acknowledge the OSIRIS Consortium for the use of OSIRIS and the visXD framework. Simulations were performed on the π supercomputer at Shanghai Jiao Tong University and Tianhe 2 supercomputer at Guangzhou.

Author Contributions

M.C. conceived the idea; J.L., M.C. and M.Z. performed the PIC simulations and radiation calculations; J.L., M.C., Z.M.S. and J.V. analyzed data; J.L., M.C., Z.M.S. and J.Z. wrote the main manuscript. J.V., L.L.Y., S.M.W., L.O.S. and D.A.J. improved the manuscript. All authors commented on the manuscript and agreed on the contents.

Additional Information

Supplementary information accompanies this paper at http://www.nature.com/srep

Competing financial interests: The authors declare no competing financial interests.

How to cite this article: Luo, J. *et al.* A compact tunable polarized X-ray source based on laser-plasma helical undulators. *Sci. Rep.* **6**, 29101; doi: 10.1038/srep29101 (2016).